

1

²A SEARCH FOR LONG-LIVED, CHARGED, SUPERSYMMETRIC PARTICLES
³USING IONIZATION WITH THE ATLAS DETECTOR

4

BRADLEY AXEN

5

September 2016 – Version 0.20

6



⁸ Bradley Axen: *A Search for Long-Lived, Charged, Supersymmetric Particles using Ion-
⁹ ization with the ATLAS Detector*, Subtitle, © September 2016

¹⁰

Usually a quotation.

¹¹

Dedicated to.

₁₂ ABSTRACT

₁₃ How to write a good abstract:

₁₄ <https://plg.uwaterloo.ca/~migod/research/beck00PSLA.html>

₁₅ PUBLICATIONS

₁₆ Some ideas and figures have appeared previously in the following publications:

₁₇

₁₈ Put your publications from the thesis here. The packages `multibib` or `bibtopic`
₁₉ etc. can be used to handle multiple different bibliographies in your document.

²¹ ACKNOWLEDGEMENTS

²² Put your acknowledgements here.

²³

²⁴ And potentially a second round.

²⁵

26 CONTENTS

27	I	INTRODUCTION	1
28	1	INTRODUCTION	3
29	II	THEORETICAL CONTEXT	5
30	2	STANDARD MODEL	7
31	2.1	Particles	7
32	2.2	Interactions	8
33	2.3	Limitations	8
34	3	SUPERSYMMETRY	9
35	3.1	Motivation	9
36	3.2	Structure	9
37	3.3	Phenomenology	9
38	4	LONG-LIVED PARTICLES	11
39	4.1	Mechanisms	11
40	4.1.1	Examples in Supersymmetry	11
41	4.2	Phenomenology	11
42	4.2.1	Disimilarities to Prompt Decays	11
43	4.2.2	Characteristic Signatures	11
44	III	EXPERIMENTAL STRUCTURE AND RECONSTRUCTION	13
45	5	THE LARGE HADRON COLLIDER	15
46	5.1	Injection Chain	15
47	5.2	Design and Parameters	15
48	5.3	Luminosity	15
49	6	THE ATLAS DETECTOR	17
50	6.1	Coordinate System	17
51	6.2	Magnetic Field	17
52	6.3	Inner Detector	17
53	6.3.1	Pixel Detector	17
54	6.3.2	Semiconductor Tracker	17
55	6.3.3	Transition Radiation Tracker	17
56	6.4	Calorimetry	17
57	6.4.1	Electromagnetic Calorimeters	17
58	6.4.2	Hadronic Calorimeters	17
59	6.4.3	Forward Calorimeters	17
60	6.5	Muon Spectrometer	17
61	6.6	Trigger	17
62	6.6.1	Trigger Scheme	17
63	6.6.2	Missing Transverse Energy Triggers	17
64	7	EVENT RECONSTRUCTION	19
65	7.1	Tracks and Vertices	19

66	7.1.1	Track Reconstruction	19
67	7.1.2	Vertex Reconstruction	19
68	7.2	Jets	19
69	7.2.1	Topological Clustering	19
70	7.2.2	Jet Energy Scale	19
71	7.2.3	Jet Energy Scale Uncertainties	19
72	7.2.4	Jet Energy Resolution	19
73	7.3	Electrons	19
74	7.3.1	Electron Identification	19
75	7.4	Muons	19
76	7.4.1	Muon Identification	19
77	7.5	Missing Transverse Energy	19
78	IV	CALORIMETER RESPONSE	21
79	8	RESPONSE MEASUREMENT WITH SINGLE HADRONS	23
80	8.1	Dataset and Simulation	24
81	8.1.1	Data Samples	24
82	8.1.2	Simulated Samples	24
83	8.1.3	Event Selection	24
84	8.2	Inclusive Hadron Response	25
85	8.2.1	E/p Distribution	26
86	8.2.2	Zero Fraction	26
87	8.2.3	Neutral Background Subtraction	27
88	8.2.4	Corrected Response	28
89	8.3	Identified Particle Response	34
90	8.3.1	Decay Reconstruction	34
91	8.3.2	Identified Response	35
92	8.3.3	Additional Species in Simulation	37
93	8.4	Summary	38
94	9	JET ENERGY RESPONSE AND UNCERTAINTY	41
95	9.1	Motivation	41
96	9.2	Uncertainty Estimate	41
97	9.3	Summary	43
98	V	SEARCH FOR LONG-LIVED PARTICLES	47
99	10	LONG-LIVED PARTICLES IN ATLAS	49
100	10.1	Overview and Characteristics	49
101	10.2	Simulation	49
102	11	EVENT SELECTION	51
103	11.1	Trigger	51
104	11.2	Kinematics and Isolation	51
105	11.3	Standard Model Rejection	51
106	11.4	Ionization	51
107	11.4.1	dE/dx Calibration	51
108	11.4.2	Mass Estimation	51
109	12	BACKGROUND ESTIMATION	53

110	12.1	Background Sources	53
111	12.2	Prediction Method	53
112	12.3	Validation and Uncertainty	53
113	13	SYSTEMATIC UNCERTAINTIES AND RESULTS	55
114	13.1	Systematic Uncertainties	55
115	13.2	Final Yields	55
116	14	INTERPRETATION	57
117	14.1	Cross Sectional Limits	57
118	14.2	Mass Limits	57
119	14.3	Context for Long-Lived Searches	57
120	VI	CONCLUSIONS	59
121	15	SUMMARY AND OUTLOOK	61
122	15.1	Summary	61
123	15.2	Outlook	61
124	VII	APPENDIX	63
125	A	INELASTIC CROSS SECTION	65
126	B	APPENDIX TEST	67
127	B.1	Appendix Section Test	67
128	B.1.1	Appendix Subection Test	67
129	B.2	A Table and Listing	67
130	B.3	Some Formulas	68
131		BIBLIOGRAPHY	71

132 LIST OF FIGURES

133	Figure 1	The particle content of the Standard Model.	8
134	Figure 2	An illustration (a) of the E/p variable used throughout this paper. The red energy deposits come from the charged particle targeted for measurement, while the blue energy deposits are from nearby neutral particles and must be subtracted. The same diagram (b) for the neutral-background selection, described in Section 8.2.3.	25
135			
136			
137			
138			
139			
140	Figure 3	The E/p distribution and ratio of simulation to data for isolated tracks with (a) $ \eta < 0.6$ and $1.2 < p/\text{GeV} < 1.8$ and (b) $ \eta < 0.6$ and $2.2 < p/\text{GeV} < 2.8$	26
141			
142			
143	Figure 4	The fraction of tracks as a function (a, b) of momentum, (c, d) of interaction lengths with $E \leq 0$ for tracks with positive (on the left) and negative (on the right) charge.	27
144			
145			
146			
147	Figure 5	$\langle E/p \rangle_{\text{BG}}$ as a function of the track momentum for tracks with (a) $ \eta < 0.6$, (b) $0.6 < \eta < 1.1$, and as a function of the track pseudorapidity for tracks with (c) $1.2 < p/\text{GeV} < 1.8$, (d) $1.8 < p/\text{GeV} < 2.2$	29
148			
149			
150			
151	Figure 6	$\langle E/p \rangle_{\text{COR}}$ as a function of track momentum, for tracks with (a) $ \eta < 0.6$, (b) $0.6 < \eta < 1.1$, (c) $1.8 < \eta < 1.9$, and (d) $1.9 < \eta < 2.3$	30
152			
153			
154	Figure 7	$\langle E/p \rangle_{\text{COR}}$ calculated using LCW-calibrated topological clusters as a function of track momentum for tracks with (a) zero or more associated topological clusters or (b) one or more associated topological clusters.	31
155			
156			
157			
158	Figure 8	Comparison of the $\langle E/p \rangle_{\text{COR}}$ for tracks with (a) less than and (b) greater than 20 hits in the TRT.	32
159			
160	Figure 9	Comparison of the $\langle E/p \rangle_{\text{COR}}$ for (a) positive and (b) negative tracks as a function of track momentum for tracks with $ \eta < 0.6$	32
161			
162			
163	Figure 10	Comparison of the E/p distributions for (a) positive and (b) negative tracks with $0.8 < p/\text{GeV} < 1.2$ and $ \eta < 0.6$, in simulation with the FTFP_BERT and QGSP_BERT physics lists.	33
164			
165			
166			
167	Figure 11	Comparison of the response of the hadronic calorimeter as a function of track momentum (a) at the EM-scale and (b) after the LCW calibration.	33
168			
169			
170	Figure 12	Comparison of the response of the EM calorimeter as a function of track momentum (a) at the EM-scale and (b) with the LCW calibration.	34
171			
172			

173	Figure 13	The reconstructed mass peaks of (a) K_S^0 , (b) Λ , and (c) $\bar{\Lambda}$ candidates.	35
174			
175	Figure 14	The E/p distribution for isolated (a) π^+ , (b) π^- , (c) proton, and (d) anti-proton tracks.	36
176			
177	Figure 15	The fraction of tracks with $E \leq 0$ for identified (a) π^+ and π^- , and (b) proton and anti-proton tracks	36
178			
179	Figure 16	The difference in $\langle E/p \rangle$ between (a) π^+ and π^- (b) p and π^+ , and (c) \bar{p} and π^-	37
180			
181	Figure 17	$\langle E/p \rangle_{\text{COR}}$ as a function of track momentum for (a) π^+ tracks and (b) π^- tracks.	38
182			
183	Figure 18	The ratio of the calorimeter response to single parti- cles of various species to the calorimeter response to π^+ with the physics list FTFP_BERT.	38
184			
185	Figure 19	The spectra of true particles inside anti- k_t , $R = 0.4$ jets with (a) $90 < p_T/\text{GeV} < 100$, (b) $400 < p_T/\text{GeV} <$ 500 , and (c) $1800 < p_T/\text{GeV} < 2300$	42
186			
187	Figure 20	The jet energy scale uncertainty contributions, as well as the total jet energy scale uncertainty, as a function of jet p_T for (a) $ \eta < 0.6$ and (b) $0.6 < \eta < 1.1$	44
188			
189	Figure 21	The jet energy scale correlations as a function of jet p_T and $ \eta $ for jets in the central region of the detector.	45
190			
191			
192			
193			

¹⁹⁴ LIST OF TABLES

¹⁹⁵ Table 1	Autem usu id	67
------------------------	------------------------	----

¹⁹⁶ LISTINGS

¹⁹⁷ Listing 1	A floating example (<code>listings</code> manual)	68
--------------------------	--	----

198 ACRONYMS

199 EG Example

200

PART I

201

INTRODUCTION

202

You can put some informational part preamble text here.

1

203

204 INTRODUCTION

205

PART II

206

THEORETICAL CONTEXT

207

You can put some informational part preamble text here.

2

208

209 STANDARD MODEL

210 The Standard Model of particle physics seeks to explain the symmetries and in-
211 teractions of all currently discovered fundamental particles. It has been tested by
212 several generations of experiments and has been remarkably successful, no sig-
213 nificant deviations have been found. The Standard Model provides predictions
214 in particle physics for interactions up to the Planck scale (10^{15} - 10^{19} GeV).

215 The theory itself is a quantum field theory grown from an underlying $SU(3) \times$
216 $SU(2) \times U(1)$ that requires the particle content and quantum numbers consist-
217 ent with experimental observations (see Section 2.1). Each postulated symme-
218 try is accompanied by an interaction between particles through gauge invari-
219 ance. These interactions are referred to as the Strong, Weak, and Electromag-
220 netic forces, which are discussed in Section 2.2.

221 Although this model has been very predictive, the theory is incomplete; for
222 example, it is not able to describe gravity or astronomically observed dark matter.
223 These limitations are discussed in more detail in Section 2.3.

224 21 PARTICLES

225 The most familiar matter in the universe is made up of protons, neutrons, and
226 electrons. Protons and neutrons are composite particles, however, and are made
227 up in turn by particles called quarks. Quarks carry both electric charge and color
228 charge, and are bound in color-neutral combinations called baryons. The elec-
229 tron is an example of a lepton, and carries only electric charge. Another type
230 of particle, the neutrino, does not form atomic structures in the same way that
231 quarks and leptons do because it carries no color or electric charge. Collectively,
232 these types of particles are known as fermions, the group of particles with half-
233 integer spin.

234 There are three generations of fermions, although familiar matter is formed
235 predominantly by the first generation. The generations are identical except for
236 their masses, which increase in each generation by convention. In addition, each
237 of these particles is accompanied by an antiparticle, with opposite-sign quantum
238 numbers but the same mass.

239 The fermions comprise what is typically considered matter, but there are
240 additional particles that are mediators of interactions between those fermions.
241 These mediators are known as the gauge bosons, gauge in that their existence
242 is required by gauge invariance (discussed further in Section 2.2) and bosons in
243 that they have integer spin. The boson which mediates the electromagnetic force
244 is the photon, the first boson to be discovered; it has no electric charge, no mass,
245 and a spin of 1. There are three spin-1 mediators of the weak force, the two W
246 bosons and the Z boson. The W bosons have electric charge of ± 1 and a mass of
247 80.385 ± 0.015 GeV, while the Z boson is neutral and has a mass of $91.1876 \pm$

248 0.0021 GeV. The strong force is mediated by eight particles called gluons, which
 249 are massless and electrically neutral but do carry color charge.

250 The final particle present in the Standard Model is the Higgs boson, which was
 251 recently observed for the first time by experiments at CERN in 2012. It is electro-
 252 cally neutral, has a mass of 125.7 ± 0.4 GeV, and is the only spin-0 particle yet to
 253 be observed. The Higgs boson is the gauge boson associated with the mechanism
 254 that gives a mass to the W and Z bosons.

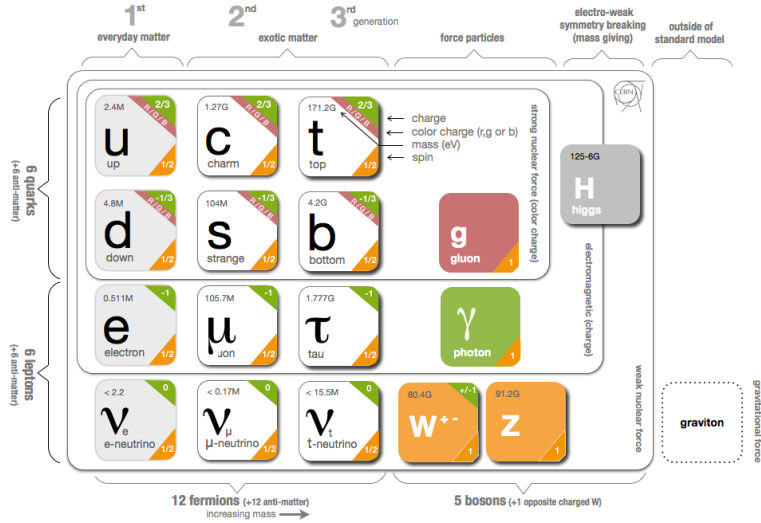


Figure 1: The particle content of the Standard Model.

255 Together these particles form the entire content of the Standard Model, and
 256 are summarized in Figure 1. These are the particles that constitute the observable
 257 universe and all the so-far-observed interactions within it.

258 2.2 INTERACTIONS

259 The interactions predicted and described by the Standard Model are fundamen-
 260 tally tied to the particles within it, both in that they describe the way those par-
 261 ticles can influence each other and also in that the existence of the interactions
 262 requires the existence of some particles (the gauge bosons).

263 2.3 LIMITATIONS

3

264

265 SUPERSYMMETRY

266 3.1 MOTIVATION

267 3.2 STRUCTURE

268 3.3 PHENOMENOLOGY

4

269

270 LONG-LIVED PARTICLES

271 4.1 MECHANISMS

272 4.1.1 EXAMPLES IN SUPERSYMMETRY

273 4.2 PHENOMENOLOGY

274 4.2.1 DISIMILARITIES TO PROMPT DECAYS

275 4.2.2 CHARACTERISTIC SIGNATURES

276

PART III

277

EXPERIMENTAL STRUCTURE AND RECONSTRUCTION

278

You can put some informational part preamble text here.

5

279

280 THE LARGE HADRON COLLIDER

281 5.1 INJECTION CHAIN

282 5.2 DESIGN AND PARAMETERS

283 5.3 LUMINOSITY

6

284

285 THE ATLAS DETECTOR

286 6.1 COORDINATE SYSTEM

287 6.2 MAGNETIC FIELD

288 6.3 INNER DETECTOR

289 6.3.1 PIXEL DETECTOR

290 6.3.2 SEMICONDUCTOR TRACKER

291 6.3.3 TRANSITION RADIATION TRACKER

292 6.4 CALORIMETRY

293 6.4.1 ELECTROMAGNETIC CALORIMETERS

294 6.4.2 HADRONIC CALORIMETERS

295 6.4.3 FORWARD CALORIMETERS

296 6.5 MUON SPECTROMETER

297 6.6 TRIGGER

298 6.6.1 TRIGGER SCHEME

299 6.6.2 MISSING TRANSVERSE ENERGY TRIGGERS

7

300

301 EVENT RECONSTRUCTION

302 The ATLAS experiment combines measurements in the subdetectors to form a
303 cohesive picture of each physics event.

304 7.1 TRACKS AND VERTICES

305 7.1.1 TRACK RECONSTRUCTION

306 7.1.1.1 NEURAL NETWORK

307 7.1.1.2 PIXEL DE/DX

308 7.1.2 VERTEX RECONSTRUCTION

309 7.2 JETS

310 7.2.1 TOPOLOGICAL CLUSTERING

311 7.2.2 JET ENERGY SCALE

312 7.2.3 JET ENERGY SCALE UNCERTAINTIES

313 7.2.4 JET ENERGY RESOLUTION

314 7.3 ELECTRONS

315 7.3.1 ELECTRON IDENTIFICATION

316 7.4 MUONS

317 7.4.1 MUON IDENTIFICATION

318 7.5 MISSING TRANSVERSE ENERGY

319

PART IV

320

CALORIMETER RESPONSE

321

You can put some informational part preamble text here.

322

323 RESPONSE MEASUREMENT WITH SINGLE HADRONS

324 As discussed in Section 7.2, colored particles produced in collisions hadronize
325 into jets of multiple individual hadrons. One approach to understanding jet physics
326 in the ATLAS calorimetry is to evaluate the calorimeter response to those indi-
327 vidual hadrons; measurements of individual hadrons can be used to build up
328 an understanding of the jets that they form. The redundancy of the momentum
329 provided by the tracking system and the energy provided by the calorimeter pro-
330 vides an opportunity to study calorimeter response using real collisions, as de-
331 scribed further in Section 8.2.

332 A number of interesting factors compromise calorimeter response, and ex-
333 tracting these separately provides insight into many aspects of jet modeling. First,
334 many charged hadrons interact with the material of the detector prior to reach-
335 ing the calorimeters and thus do not deposit any energy. Comparing this effect in
336 data and simulation is a powerful tool in validating the interactions of particles
337 with the material of the detector as well as the model of the detector geometry
338 in simulation, see Section 8.2.2. The particles which do reach the calorimeter de-
339 posit their energy into individual cells, which are then clustered to measure full
340 energy deposits. Comparing the response in data to simulated hadrons provides
341 a direct evaluation of several aspects of simulation: noise in the calorimeters, the
342 showering of hadronic particles, and the energy deposited by particles in mat-
343 ter, among others (Section 8.2.4). These measurements are extended to explore
344 several additional effects, such as the dependence on charge, in Section 8.2.4.1.

345 The above studies all use an inclusive selection of charged particles, which are
346 compromised predominantly of pions, kaons, and (anti)protons. It is also inter-
347 esting to measure the particle types separately to evaluate the simulated inter-
348 actions of each particle, particularly at low energies where differences between
349 species are very relevant. Pions and (anti)protons can be identified through de-
350 cays of long-lived particles, in particular Λ , $\bar{\Lambda}$, and K_S^0 , and then used to measure
351 response as described above. This is discussed in detail in Section 8.3.

352 Together, these measurements in data provide a thorough understanding of
353 the way hadrons interact with the ATLAS detector and can be used to build up a
354 description of jets, as seen in Chapter 9. The results in this chapter use data col-
355 lected at 7 and 8 TeV collected in 2010 and 2012, respectively. Both are included
356 as the calorimeter was repaired and recalibrated between those two data-taking
357 periods. Both sets of data are compared to an updated simulation that includes
358 new physics models provided by Geant4 [12] and improvements in the detector
359 description [2, 6]. These results are published in EPJC [8] and can be compared to
360 a similar measurement performed in 2009 and 2010 [5], which used the previous
361 version of the simulation framework [1].

362 8.1 DATASET AND SIMULATION

363 8.1.1 DATA SAMPLES

364 The two datasets used in this chapter are taken from dedicated low-pileup runs
 365 where the fraction of events with multiple interactions was negligible, to facilitate
 366 measurement of isolated hadrons. The 2012 dataset at $\sqrt{s} = 8$ TeV contains
 367 8 million events and corresponds to an integrated luminosity of 0.1 nb^{-1} . The
 368 2010 dataset at $\sqrt{s} = 7$ TeV contains 3 million events and corresponds to an
 369 integrated luminosity of 3.2 nb^{-1} . This last dataset was also used in the 2010 re-
 370 sults [5], but it has since been reanalyzed with an updated detector description
 371 for the material and alignment.

372 8.1.2 SIMULATED SAMPLES

373 The two datasets above are compared to simulated single-, double-, and non-
 374 diffractive events generated with Pythia8 [32] using the A2 configuration of
 375 hadronization [3] and the MSTW 2008 parton-distribution function set [28, 31].
 376 The conditions and energies for each run are matched in the two simulations.

377 To evaluate the interaction of hadrons with detector material, the simulation
 378 uses two different collections of hadronic physics models, called physics lists, in
 379 Geant4 9.4 [30]. The first, QGSP_BERT, combines the Bertini intra-nuclear
 380 cascade [17, 24, 26] below 9.9 GeV, a parametrized proton inelastic model from
 381 9.5 to 25 GeV [21], and a quark-gluon string model above 12 GeV [13, 14, 18, 19,
 382 22]. The second, FTFP_BERT, combines the Bertini intra-nuclear cascade [17, 24,
 383 26] below 5 GeV and the Fritiof model [15, 16, 23, 29] above 4 GeV. In either list,
 384 Geant4 enforces a smooth transition between models where multiple models
 385 overlap.

386 8.1.3 EVENT SELECTION

387 The event selection for this study is minimal, as the only requirement is selecting
 388 good-quality events with an isolated track. Such events are triggered by requir-
 389 ing at least two hits in the minimum-bias trigger scintillators. After trigger, each
 390 event is required to have exactly one reconstructed vertex, and that vertex is re-
 391 quired to have four or more associated tracks.

392 The particles which enter into the response measurements are first identified
 393 as tracks in the inner detector. To ensure a reliable momentum measurement,
 394 these tracks are required to have at least one hit in the pixel detector, six hits in
 395 the SCT, and small longitudinal and transverse impact parameters with respect
 396 to the primary vertex [5]. For the majority of the measurements in this chap-
 397 ter, the track is additionally required to have 20 hits in the TRT, which signifi-
 398 cantly reduces the contribution from tracks which undergo nuclear interactions.
 399 This requirement and its effect is discussed in more detail in Section 8.2.4.1. In
 400 addition, tracks are rejected if there is another track which extrapolates to the
 401 calorimeter within a cone of $\Delta R = \sqrt{(\Delta\phi)^2 + (\Delta\eta)^2} < 0.4$. This requirement

402 guarantees that the contamination of energy from nearby charged particles is
 403 negligible [5].

404 8.2 INCLUSIVE HADRON RESPONSE

405 The calorimeter response is more precisely defined as the ratio of the measured
 406 calorimeter energy to the true energy carried by the particle, although this true
 407 energy is unknown. For charged particles, however, the inner detector provides
 408 a very precise measurement of momentum (with uncertainty less than 1%) that
 409 can be used as a proxy for true energy. The ratio of the energy deposited by the
 410 charged particle in the calorimeter, E , to its momentum measured in the inner
 411 detector p , forms the calorimeter response measure called E/p . Though the dis-
 412 tribution of E/p is interesting, two aggregated quantities are more directly use-
 413 ful: $\langle E/p \rangle$, the average of E/p within a given subset of particles, and the zero
 414 fraction, the fraction of particles with no associated energy in the calorimeter.

415 The calorimeter energy assigned to a track particle is defined using clusters.
 416 The clusters are formed using a 4–2–0 algorithm [9] that begins with seeds re-
 417 quiring at least 4 times the average calorimeter noise. The neighboring cells with
 418 at least twice that noise threshold are then added to the cluster, and all bound-
 419 ing cells are then added with no requirement. This algorithm minimizes noise
 420 contributions through its seeding process, and including the additional layers
 421 improves the energy resolution [33]. The clusters are associated to a given track
 422 if they fall within a cone of $\Delta R = 0.2$ of the extrapolated position of the track,
 423 which includes about 90% of the energy on average [5]. This construction is il-
 424 lustrated in Figure 2.

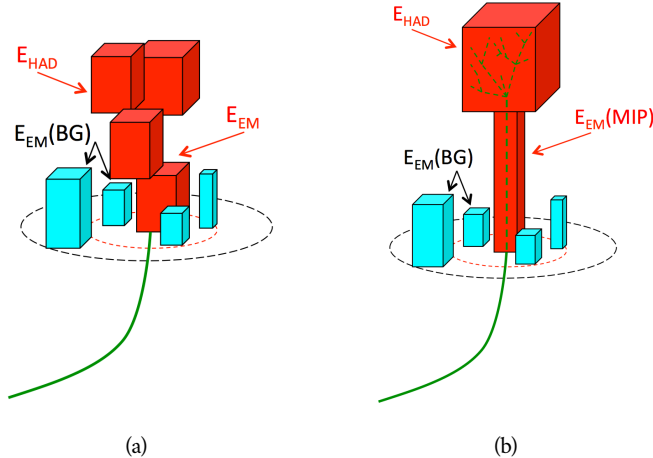
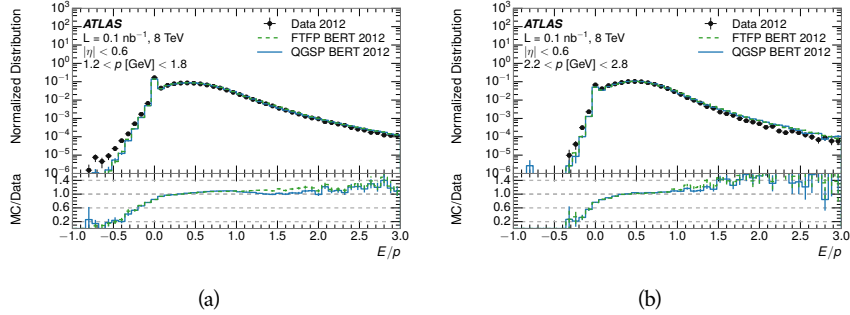


Figure 2: An illustration (a) of the E/p variable used throughout this paper. The red energy deposits come from the charged particle targeted for measurement, while the blue energy deposits are from nearby neutral particles and must be subtracted. The same diagram (b) for the neutral-background selection, described in Section 8.2.3.

425 8.2.1 E/P DISTRIBUTION

426 The E/p distributions measured in both data and simulation are shown in Figure 3 for two example bins of track momentum and for tracks in the central
 427 region of the detector. These distributions show several important features of
 428 the E/p observable. The large content in the bin at $E = 0$ comes from tracks that
 429 have no associated cluster, which occurs due to interactions with detector mate-
 430 rial prior to reaching the calorimeter or the energy deposit being insufficiently
 431 large to generate a seed, and are discussed in Section 8.2.2. The small negative
 432 tail comes from similar tracks that do not deposit any energy in the calorimeter
 433 but are randomly associated to a noise cluster. The long positive tail above 1.0
 434 comes from the contribution of neutral particles. Nearby neutral particles de-
 435 posit (sometimes large) additional energy in the calorimeter but do not produce
 436 tracks in the inner detector, so they cannot be rejected for isolation. Additionally
 437 the peak and mean of the distribution falls below 1.0 because of the loss of energy
 438 not found within the cone as well as the non-compensation of the calorimeter.
 439

440 The data and simulation share the same features, but the high and low tails
 441 are significantly different. The simulated events tend to overestimate the contri-
 442 bution of neutral particles to the long tail, an effect which can be isolated and
 443 removed as discussed in Section 8.2.3. Additionally, the simulated clusters have
 444 less noise on average, although this is a small effect on the overall response.



445 Figure 3: The E/p distribution and ratio of simulation to data for isolated tracks with
 446 (a) $|\eta| < 0.6$ and $1.2 < p/\text{GeV} < 1.8$ and (b) $|\eta| < 0.6$ and $2.2 < p/\text{GeV} < 2.8$.

445 8.2.2 ZERO FRACTION

446 The fraction of particles with no associated clusters, or similarly those with $E \leq$
 447 0, reflects the modeling of both the detector geometry and hadronic interactions.
 448 The zero fraction is expected to rise as the amount of material a particle traverses
 449 increases, while it is expected to decrease as the particle energy increases. This
 450 dependence can be seen in Figure 4, where the zero fraction in data and simula-
 451 tion is shown as a function of momentum and the amount of material measured
 452 in interaction lengths. The trends are similar between the 2010 and 2012 mea-
 453 surements. The zero fraction decreases with energy as expected. The amount of
 454 material in the detector increases with η , which provides a distribution of inter-

action lengths. As the data and simulation have significant disagreement in the zero fraction over a number of interaction lengths, the difference must be primarily from the modeling of hadronic interactions with detector material and not just the detector geometry.

There is also a noticeable difference between positive and negative tracks at low momentum, which reflects the difference in response between protons and antiprotons. Antiprotons have significant model differences in the two physics lists, QGSP_BERT and FTFP_BERT, and this is evident in the lowest momentum bin of the data to simulation ratio. This difference is explored further in Section 8.3.

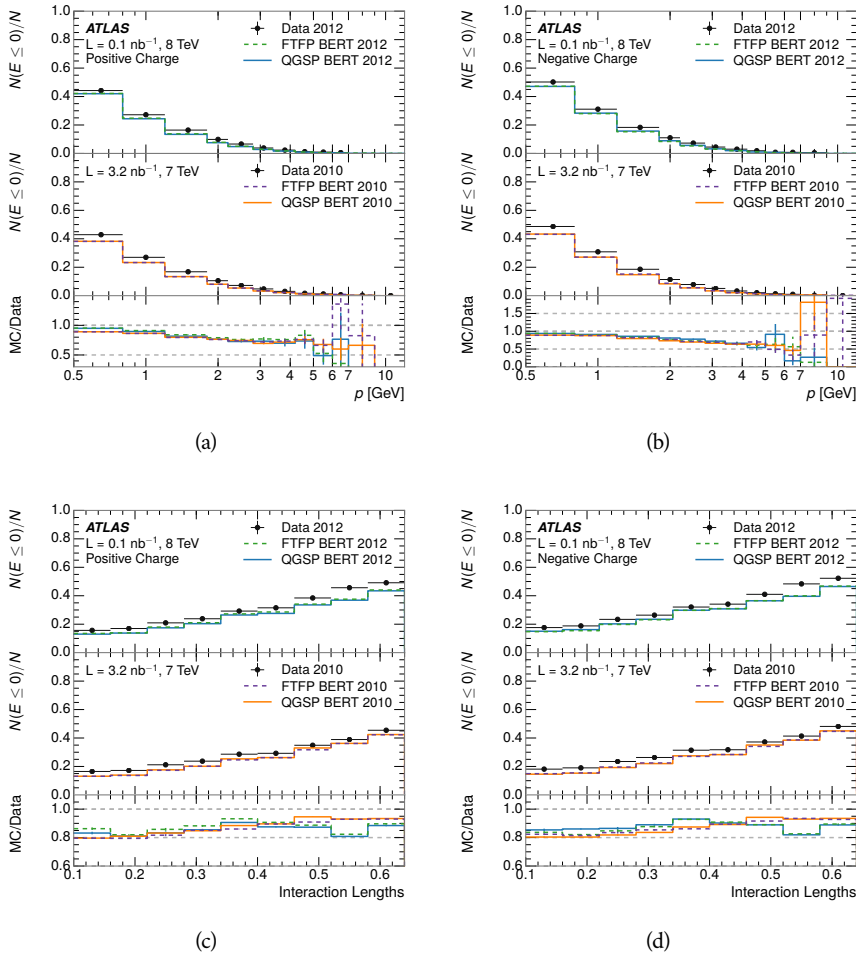


Figure 4: The fraction of tracks as a function (a, b) of momentum, (c, d) of interaction lengths with $E \leq 0$ for tracks with positive (on the left) and negative (on the right) charge.

8.2.3 NEUTRAL BACKGROUND SUBTRACTION

The isolation requirement on hadrons is only effective in remove energy contribution from nearby charged particles. Nearby neutral particles, predominantly

468 photons from π^0 decays, also add their energy to the calorimeter clusters, but
 469 mostly in the electromagnetic calorimeter. It is possible to measure this contribu-
 470 tion, on average, using late-showering hadrons that minimally ionize in the
 471 electromagnetic calorimeter. Such particles are selected by requiring that they
 472 deposit less than 1.1 GeV in the EM calorimeter within a cone of $\Delta R < 0.1$
 473 around the track. To ensure that these particles are well measured, they are addi-
 474 tionally required to deposit between 40% and 90% of their energy in the hadronic
 475 calorimeter within the same cone.

476 These particles provide a clean sample to measure the nearby neutral back-
 477 ground because they do not deposit energy in the area immediately surrounding
 478 them in the EM calorimeter, as shown in Figure 2. So, the energy deposits in the
 479 region $0.1 < \Delta R < 0.2$ can be attributed to neutral particles alone. To estimate
 480 the contribution to the whole cone considered for the response measurement,
 481 that energy is scaled by a geometric factor of 4/3. This quantity, $\langle E/p \rangle_{\text{BG}}$, mea-
 482 sured in aggregate over a number of particles, gives the contribution to $\langle E/p \rangle$
 483 from neutral particles in the EM calorimeter. Similar techniques were used in
 484 the individual layers of the hadronic calorimeters to show that the background
 485 from neutrals is negligible in those layers [5].

486 The distribution of this background estimate is shown in Figure 5. Although
 487 the simulation captures the overall trend, it significantly overestimates the neu-
 488 tral contribution for tracks with momentum between 2 and 8 GeV. This effect
 489 was also seen in the tails of the E/p distributions in Figure 3. This difference is
 490 likely due to the modeling of coherent neutral particle radiation in Pythia8, as
 491 the discrepancy does not depend on η and thus is unlikely to be a mismodeling
 492 of the detector. This difference can be subtracted to form a corrected average
 493 E/p , as in Section 8.2.4.

494 8.2.4 CORRECTED RESPONSE

495 Figure 6 shows $\langle E/p \rangle_{\text{COR}}$ as a function of momentum for several bins of pseu-
 496 dorapidity. This corrected $\langle E/p \rangle_{\text{COR}} \equiv \langle E/p \rangle - \langle E/p \rangle_{\text{BG}}$ measures the average
 497 calorimeter response without the contamination of neutral particles. It is the
 498 most direct measurement of calorimeter response in that it is the energy mea-
 499 sured for fully isolated hadrons. The correction is performed separately in data
 500 and simulation, so that the mismodeling of the neutral background in simulation
 501 is removed from the comparison of response. The simulation overestimates the
 502 response at low momentum by about 5%, an effect that can be mostly attributed
 503 to the underestimation of the zero fraction mentioned previously.

504 The response measurement above used topological clustering at the EM scale,
 505 that is clusters were formed to measure energy but no corrections were applied
 506 to correct for expected effects like energy lost outside of the cluster or in unin-
 507 strumented material. It is also interesting to measure $\langle E/p \rangle_{\text{COR}}$ using local clus-
 508 ter weighted (LCW) energies, which accounts for those effects by calibrating the
 509 energy based on the properties of the cluster such as energy density and depth
 510 in the calorimeter. Figure 7 shows these distributions for tracks with zero or
 511 more clusters and separately for tracks with one or more clusters. The calibra-

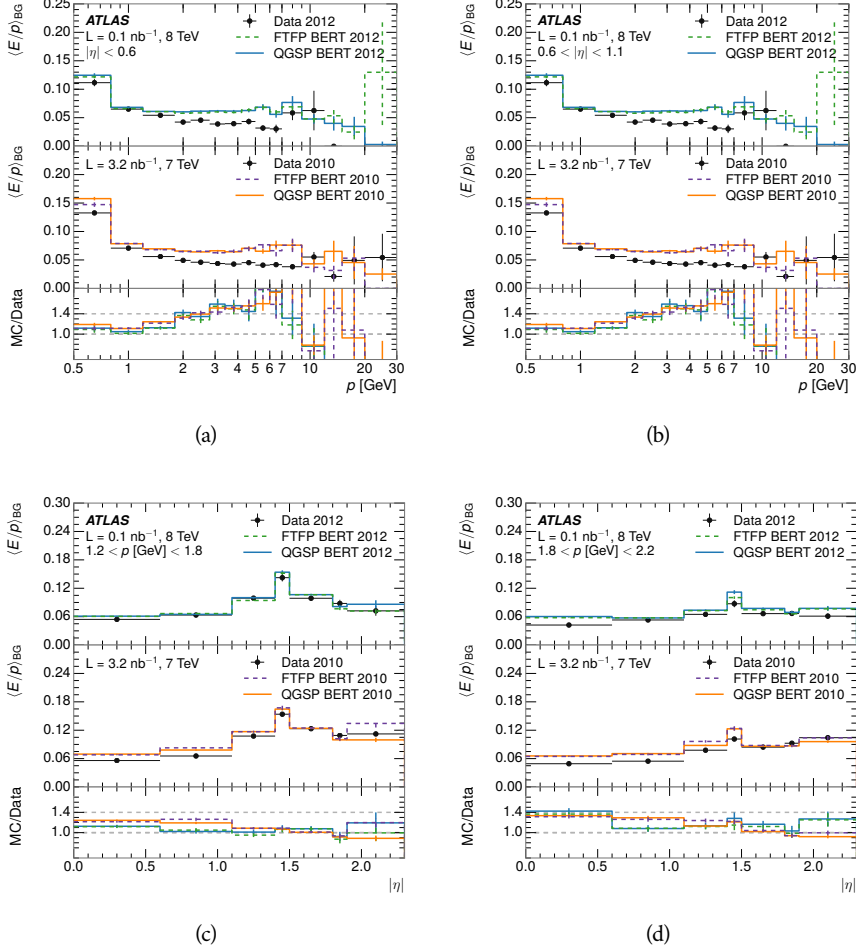


Figure 5: $\langle E/p \rangle_{BG}$ as a function of the track momentum for tracks with (a) $|\eta| < 0.6$, (b) $0.6 < |\eta| < 1.1$, and as a function of the track pseudorapidity for tracks with (c) $1.2 < p/\text{GeV} < 1.8$, (d) $1.8 < p/\text{GeV} < 2.2$.

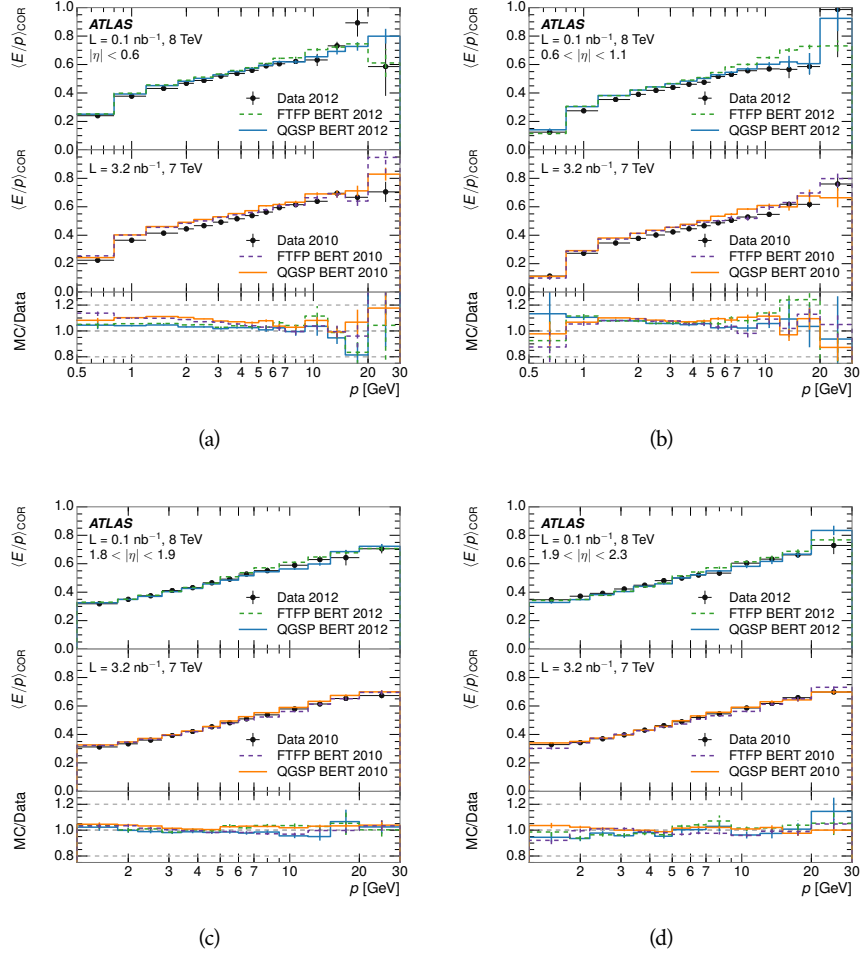


Figure 6: $\langle E/p \rangle_{\text{COR}}$ as a function of track momentum, for tracks with (a) $|\eta| < 0.6$, (b) $0.6 < |\eta| < 1.1$, (c) $1.8 < |\eta| < 1.9$, and (d) $1.9 < |\eta| < 2.3$.

tion moves $\langle E/p \rangle_{\text{COR}}$ significantly closer to 1.0, which is the purpose of the calibration. The agreement between data and simulation improves noticeably when at least one cluster is required, as this removes the contribution from the mismodeling of zero fraction.

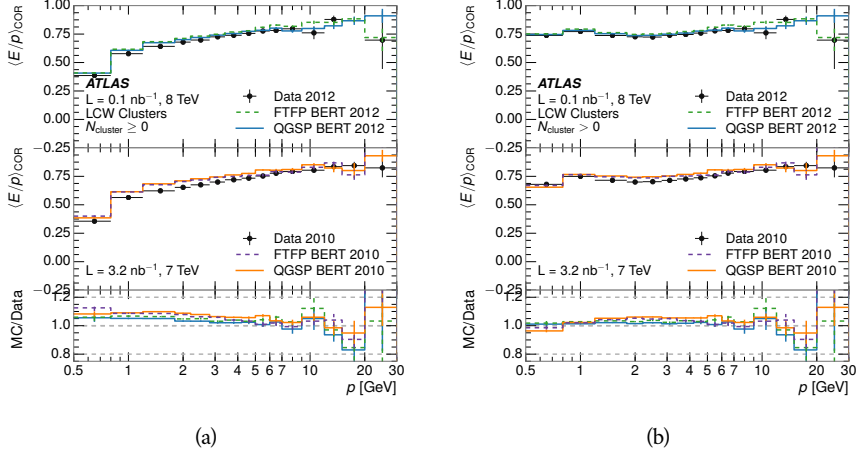


Figure 7: $\langle E/p \rangle_{\text{COR}}$ calculated using LCW-calibrated topological clusters as a function of track momentum for tracks with (a) zero or more associated topological clusters or (b) one or more associated topological clusters.

8.2.4.1 ADDITIONAL STUDIES

As has been seen in several previous measurements, the simulation does not correctly model the chance of a low momentum hadron to reach the calorimeter. Because of the consistent discrepancy across pseudorapidity and interaction lengths, this seems to be best explained by incomplete understanding of hadronic interactions with the detector. For example, a hadron that scatters off of a nucleus in the inner detector can be deflected through a significant angle and not reach the expected location in the calorimeter. In addition, these interaction can produce secondary particles that are difficult to model.

The requirement on the number of hits in the TRT reduces these effects by preferentially selecting tracks that do not undergo nuclear interactions. It is interesting to check how well the simulation models tracks with low numbers of TRT hits, where the nuclear interactions are much more likely. Figure 8 compares the distributions with $N_{\text{TRT}} < 20$ to $N_{\text{TRT}} > 20$ for real and simulated particles. As expected, the tracks with fewer hits are poorly modeled in the simulation as $\langle E/p \rangle_{\text{COR}}$ differs by as much as 25% at low momentum.

Another interesting aspect of the simulation is the description of antiprotons at low momentum, where QGSP_BERT and FTFP_BERT have significant differences. This can be seen to have an effect in the inclusive response measurement when separated into positive and negative charge. The $\langle E/p \rangle_{\text{COR}}$ distributions for positive and negative particles are shown in Figure 9, where a small difference between QGSP_BERT and FTFP_BERT can be seen in the distribution for negative tracks. This is demonstrated more clearly in Figure 10, which shows

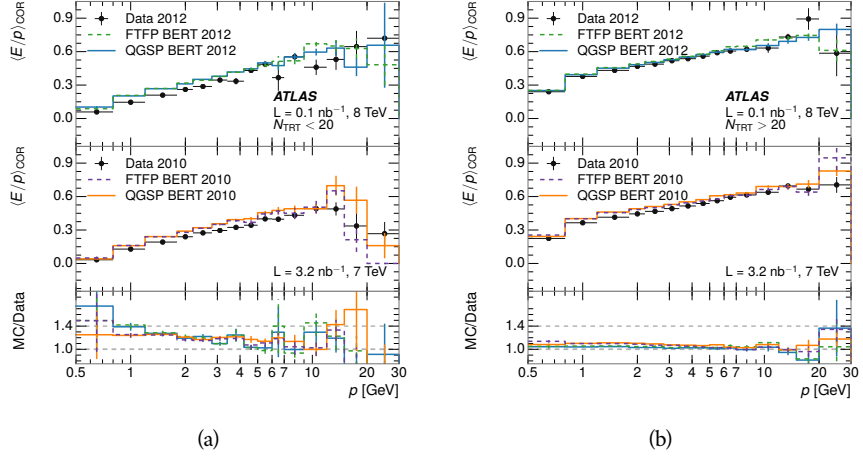


Figure 8: Comparison of the $\langle E/p \rangle_{\text{COR}}$ for tracks with (a) less than and (b) greater than 20 hits in the TRT.

the E/p distribution in the two simulations separated by charge. There is a clear difference around $E/p > 1.0$, which can be explained by the additional energy deposited by the annihilation of the antiproton in the calorimeter that is modeled well only in FTFP_BERT. This is also explored with data using identified antiprotons in Section 8.3.

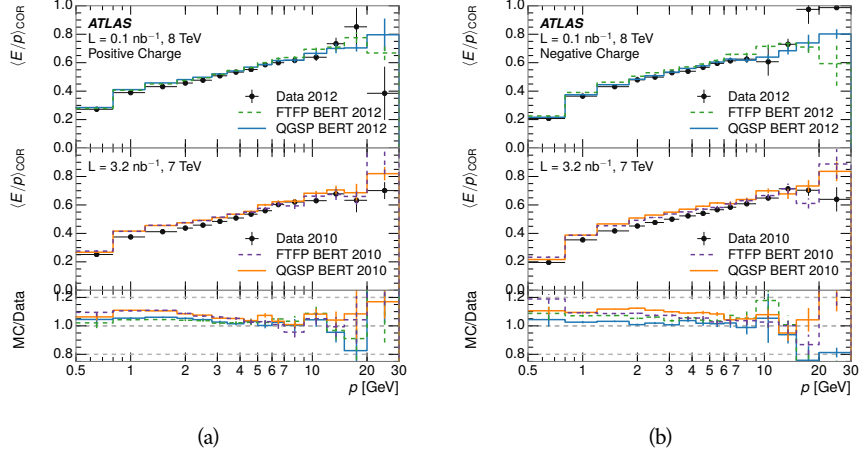


Figure 9: Comparison of the $\langle E/p \rangle_{\text{COR}}$ for (a) positive and (b) negative tracks as a function of track momentum for tracks with $|\eta| < 0.6$.

The $\langle E/p \rangle$ results in previous sections have considered the electromagnetic and hadronic calorimeters together as a single energy measurement, to emphasize the total energy deposited for a given particle. However, the deposits in each calorimeter are available separately and $\langle E/p \rangle$ can be constructed for each layer. As the layers are composed of different materials and are modeled separately in the detector geometry, confirm that the simulation matches the data well in each

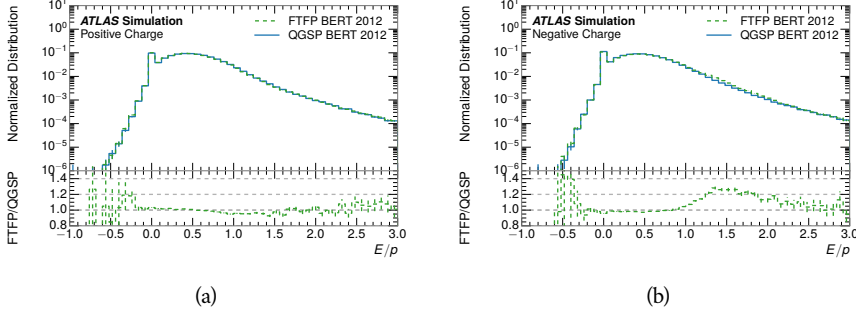


Figure 10: Comparison of the E/p distributions for (a) positive and (b) negative tracks with $0.8 < p/\text{GeV} < 1.2$ and $|\eta| < 0.6$, in simulation with the FTFP_BERT and QGSP_BERT physics lists.

layer adds confidence in both the description of hadronic interactions with the two different materials and also the geometric description of each.

The technique discussed in Section 8.2.3 for selection minimally ionizing particles (MIPs) in the electromagnetic calorimeter is also useful in studying deposits in the hadronic calorimeter. Those MIPs deposit almost all of their energy exclusively in the hadronic calorimeter. Figure 11 shows $\langle E/p \rangle_{\text{RAW}}^{\text{Had}}$, where RAW indicates that no correction has been applied for neutral backgrounds and Had indicates that only clusters for the hadronic calorimeter are included. The RAW and COR versions of $\langle E/p \rangle$ in this case are the same, as the neutral background is negligible in that calorimeter layer. The distributions are shown both for the original EM scale calibration and after LCW calibration. The data and simulation agree very well in this comparison, except in the lowest momentum bin which has 5% discrepancy that has been reflected in similar results.

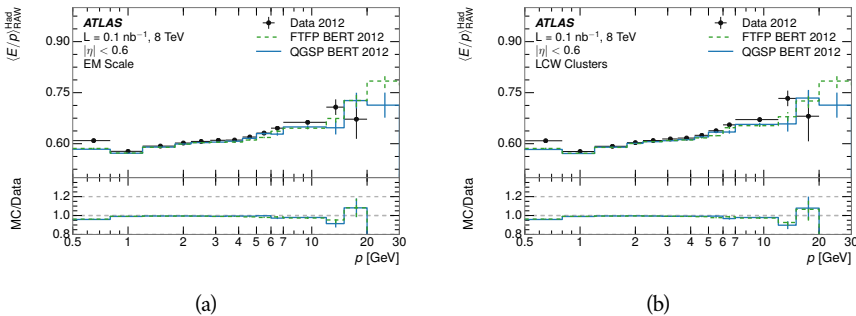


Figure 11: Comparison of the response of the hadronic calorimeter as a function of track momentum (a) at the EM-scale and (b) after the LCW calibration.

A similar comparison can be made in the electromagnetic calorimeter by selecting particles which have no associated energy in the hadronic calorimeter. These results are measured in terms of $\langle E/p \rangle_{\text{COR}}^{\text{EM}}$, where EM designates that only clusters in the electromagnetic calorimeter are included and COR designates that the neutral background is subtracted as the neutral background is present in this case. Figure 12 shows the analogous comparisons to Figure 11 in the elec-

tromagnetic calorimeter. In this case the disagreement between data and simulation is more pronounced, with discrepancies as high as 5% over a larger range of momenta. This level of discrepancy indicates that the description of the electromagnetic calorimeter is actually the dominant source of discrepancy in the combined distributions in Section 8.2.4.

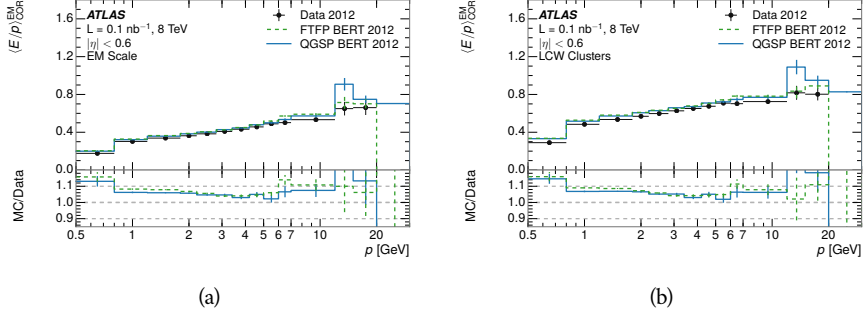


Figure 12: Comparison of the response of the EM calorimeter as a function of track momentum (a) at the EM-scale and (b) with the LCW calibration.

NOTE: There are more studies that I skipped for brevity that could be included if interesting. E/p at different cluster threshold settings, E/p with pileup, E/p with cells. I also left out a lot of eta bins that appear in the paper so that this section didn't turn into 20 pages of plots.

578 8.3 IDENTIFIED PARTICLE RESPONSE

The inclusive response measurement for hadrons can be augmented by measuring the response for specific particle species. The simulation models each particle type separately, and understanding the properties of each is important in constraining the uncertainty on jets. In order to select and measure specific hadrons, this section relies on the displaced decays of long-lived particles. Such decays can be identified by reconstructing secondary vertices, and the particles used decay predominantly to specific hadrons. In particular, Λ , $\bar{\Lambda}$, and K_S^0 can be used to select a pure sample of protons, antiprotons, and pions, respectively.

587 8.3.1 DECAY RECONSTRUCTION

The measurement of response for identified particles uses the same selection as for inclusive particles (Section 8.1.3) with a few additions. Each event used is required to have at least one secondary vertex, and the tracks are required to match to that vertex rather than the primary vertex. Pions are selected from decays of $K_S^0 \rightarrow \pi^+ \pi^-$, which is the dominant decay for K_S^0 to charged particles. Protons are selected from decays of $\Lambda \rightarrow \pi^- p$ and antiprotons from $\bar{\Lambda} \rightarrow \pi^+ \bar{p}$, which are similarly the dominant decays of Λ and $\bar{\Lambda}$ to charged particles. The species of parent hadron in these decays is determined by reconstructing the mass of the tracks associated to the secondary vertex. The sign of the higher

597 momentum decay particle can distinguish between Λ and $\bar{\Lambda}$, which of course
 598 have the same mass, as the proton or antiproton is kinematically favored to have
 599 higher momentum. Examples of the reconstructed masses used to select these
 600 decays are shown in Figure 13.

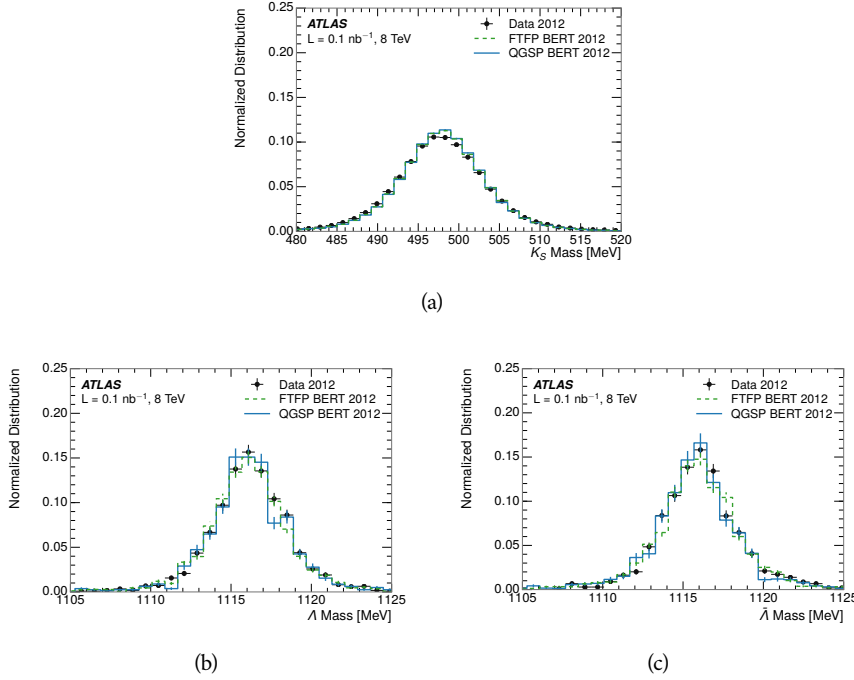


Figure 13: The reconstructed mass peaks of (a) K_S^0 , (b) Λ , and (c) $\bar{\Lambda}$ candidates.

601 There are a number of sources of backgrounds for these identified particles,
 602 including nuclear interactions and combinatoric sources. These are suppressed
 603 by the kinematic requirements on the tracks as well as an additional veto which
 604 removes candidates that are consistent with both a Λ or $\bar{\Lambda}$ and a K_S^0 hypothesis,
 605 which is possible because of the different assumptions on particle mass in each
 606 case [5]. After these requirements, the backgrounds are found to be negligible
 607 compared to the statistical errors on these measurements.

608 8.3.2 IDENTIFIED RESPONSE

609 With these techniques the E/p distributions are extracted in data and simulation
 610 for each particle species and shown in Figure 14. These distributions are shown
 611 for a particular bin of E_a ($2.2 < E_a/\text{GeV} < 2.8$), rather than p . E_a is the energy
 612 available to be deposited in the calorimeter: for pions $E_a = \sqrt{p^2 + m^2}$, for pro-
 613 tons $E_a = \sqrt{p^2 + m^2} - m$, and for antiprotons $E_a = \sqrt{p^2 + m^2} + m$. The features
 614 of the E/p distributions are similar to the inclusive case. There is a small nega-
 615 tive tail from noise and a large fraction of tracks with zero energy from tracks
 616 which do not reach the calorimeter. The long positive tail is noticeably more
 617 pronounced for antiprotons because of the additional energy generated by the
 618 annihilation in addition to the neutral background.

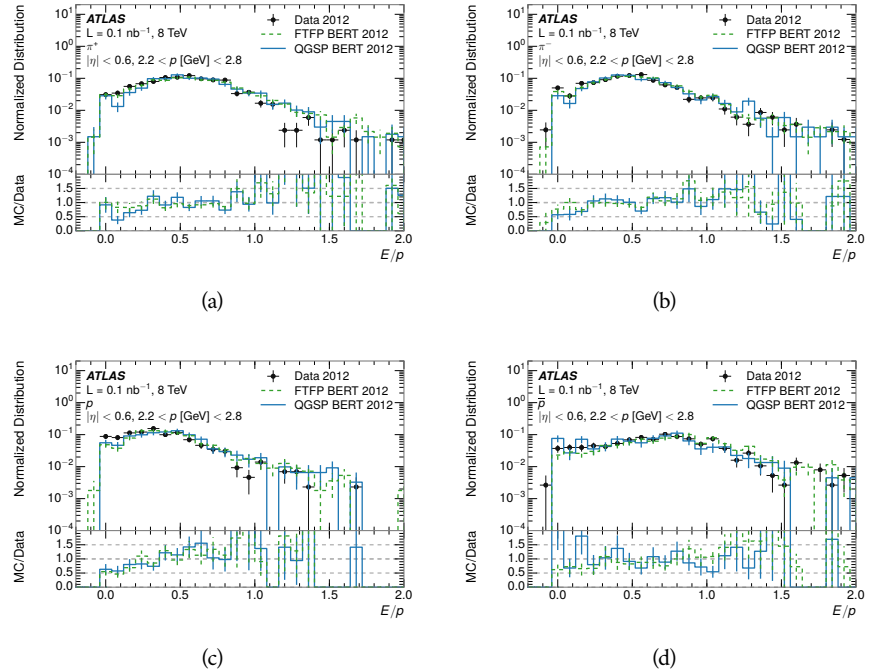


Figure 14: The E/p distribution for isolated (a) π^+ , (b) π^- , (c) proton, and (d) anti-proton tracks.

619 The zero fraction is further explored in Figure 15 for pions and protons in
 620 data and simulation. The simulation consistently underestimates the zero frac-
 621 tion independent of particle species, which implies that this discrepancy is not
 622 caused by the model of a particular species but rather a feature common to all.

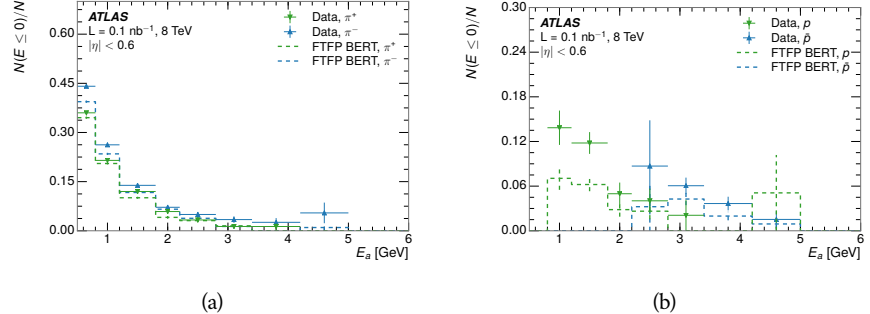


Figure 15: The fraction of tracks with $E \leq 0$ for identified (a) π^+ and π^- , and (b) proton and anti-proton tracks

623 It is also interesting to compare the response between the different particle
 624 species. One approach to do this is to measure the difference in $\langle E/p \rangle$ between
 625 two types, which has the advantage of removing the neutral background. These
 626 differences are shown in various combinations in Figure 16. The response for
 627 π^+ is greater on average than the response to π^- because of a charge-exchange
 628 effect which causes the production of additional neutral pions in the showers of
 629 π^+ [20]. The response for π^+ is also greater on average than the response to p ,

630 because a large fraction of the energy of π^+ hadrons is converted to an electro-
 631 magnetic shower [11, 25]. However, the \bar{p} response is significantly higher than
 632 the response to π^- because of the annihilation of the antiproton. FTFP_BERT
 633 does a better job of modeling this effect than QGSP_BERT because of their differ-
 634 ent descriptions of \bar{p} interactions with material.

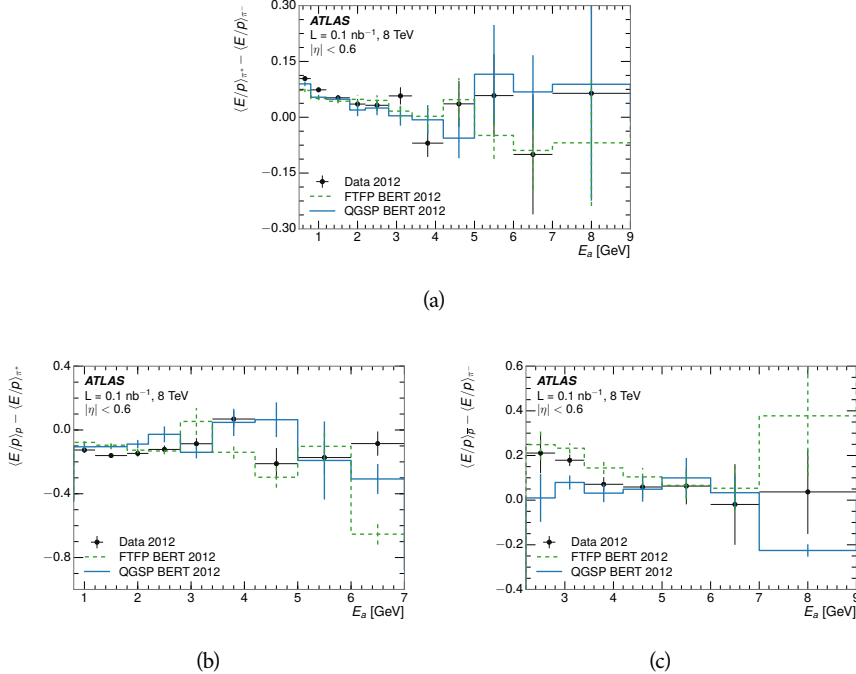


Figure 16: The difference in $\langle E/p \rangle$ between (a) π^+ and π^- (b) p and π^+ , and (c) \bar{p} and π^- .

635 It is also possible to remove the neutral background from these response dis-
 636 tributions using the same technique as in Section 8.2.3. The technique is largely
 637 independent of the particle species and so can be directly applied to $\langle E/p \rangle$ for
 638 pions. The $\langle E/p \rangle_{\text{COR}}$ distributions for pions are shown in Figure 17, which are
 639 very similar to the inclusive results. The inclusive hadrons are compromized
 640 mostly of pions, so this similarity is not surprising. It is also possible to see the
 641 small differences between π^+ and π^- response here, where $\langle E/p \rangle_{\text{COR}}$ is higher
 642 on average for π^+ . The agreement between data and simulation is significantly
 643 worse for the π^- distributions than for the π^+ , with a discrepancy greater than
 644 10% below 2-3 GeV.

645 8.3.3 ADDITIONAL SPECIES IN SIMULATION

646 The techniques above provide a method to measure the response separately only
 647 pions and protons. However the hadrons which forms jets include a number of
 648 additional species such as kaons and neutrons. The charged kaons are an impor-
 649 tant component of the inclusive charged hadron distribution, which is compro-
 650 mised of roughly 60-70% pions, 15-20% kaons, and 5-15% protons. These are dif-
 651 ficult to measure in data at the ATLAS detector, although a template subtraction

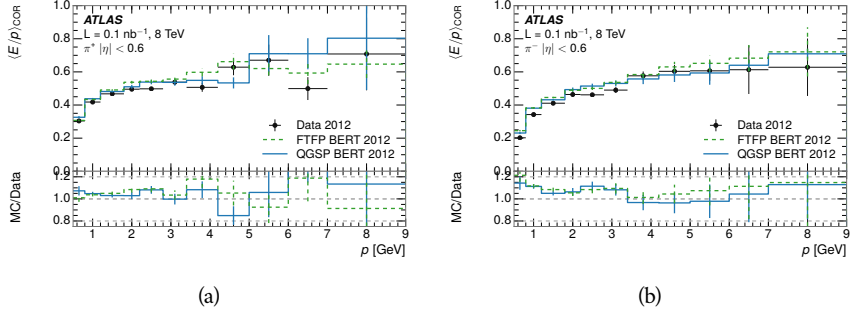


Figure 17: $\langle E/p \rangle_{\text{COR}}$ as a function of track momentum for (a) π^+ tracks and (b) π^- tracks.

technique has been proposed which may be effective with larger sample sizes [8].
The simulation of these particles includes noticeable differences in response at
low energies, which are shown in Figure 18 for FTFP_BERT. The significant differ-
ences in response between low energy protons and antiprotons are accounted
for above in the definitions of E_a .

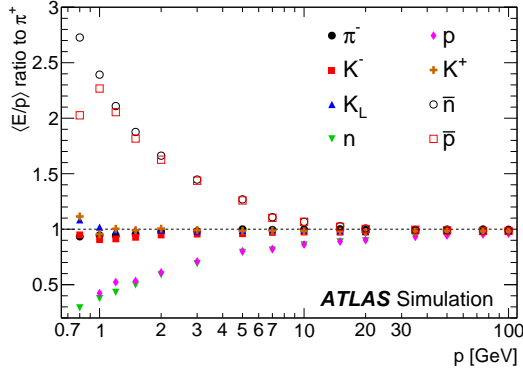


Figure 18: The ratio of the calorimeter response to single particles of various species to the calorimeter response to π^+ with the physics list FTFP_BERT.

8.4 SUMMARY

These various measurements of calorimeter response shown above for data and simulation illuminate the accuracy of the simulation of hadronic interactions at the ATLAS detector. The results were done using 2010 and 2012 data at 7 and 8 TeV, but reflect the most current understanding of the detector alignment and geometry. A number of measurements focusing on a comparison between protons and antiprotons suggest that FTFP_BERT models those interaction more accurately than QGSP_BERT. These measurements, among others, were the motivation to switch the default Geant4 simulation from FTFP_BERT to QGSP_BERT for all ATLAS samples.

Even with these updates, there are a number of small, approximately 5%, discrepancies in response between the data and simulation at low energies. At higher

669 energies the simulation of hadronic interactions is very consistent with data.
670 Chapter 9 discusses how to use these observed differences to constrain the jet
671 energy scale and its associated uncertainties.

672

673 JET ENERGY RESPONSE AND UNCERTAINTY

674 9.1 MOTIVATION

675 As jets form a major component of many physics analyses at ATLAS, it is crucial
 676 to carefully calibrate the measurement of jet energies and to derive an uncer-
 677 tainty on that measurement. These uncertainties have often been the dominant
 678 systematic uncertainty in high-energy analyses at the LHC. Dijet and multijet bal-
 679 ance techniques provide a method to constrain the jet energy scale and its uncer-
 680 tainty in data, and provide the default values used for ATLAS jet measurements
 681 at most energies [7]. These techniques are limited by their reliance on measuring
 682 jets in data, so they are statistically limited in estimating the jet energy scale at the
 683 highest jet energies. This chapter presents another method for estimating the jet
 684 energy scale and its uncertainty which builds up a jet from its components and
 685 thus can be naturally extended to high jet momentum. Throughout this chapter
 686 the jets studied are simulated using Pythia8 with the CT10 parton distribution
 687 set [27] and the AU2 tune [3], and corrections are taken from the studies includ-
 688 ing data and simulation in Chapter 8.

689 As described in Section 7.2, jets are formed from topological clusters of energy
 690 in the calorimeters using the anti- k_t algorithm. These clusters originate from a
 691 diverse spectrum of particles, in terms of both species and momentum, leading to
 692 significantly varied jet properties and response between jets of similar produced
 693 momentum. Figure 19 shows the simulated distribution of particles within jets
 694 at a few examples energies. The E/p measurements provide a thorough under-
 695 standing of the dominant particle content of jets, the charged hadrons.

696 9.2 UNCERTAINTY ESTIMATE

697 Simulated jets are not necessarily expected to correctly model the energy de-
 698 posits in the calorimeters, because of the various discrepancies discussed in Chap-
 699 ter 8. To evaluate a jet energy response, the simulated jet energies are compared
 700 to a corrected jet built up at the particle level. Each cluster in a jet is associated
 701 to the truth particle which deposited it, and the energy in that cluster is then
 702 corrected for a number of effects based on measurements in data. The primary
 703 corrections come from the single hadron response measurements in addition
 704 to response measured using the combined test beam which covers higher mo-
 705 mentum particles [10]. These corrections include both a shift, in order to make
 706 the simulation match the average response in data, and an uncertainty associated
 707 with the ability to constrain the difference between data and simulation. Some of
 708 the dominant sources of uncertainty are itemized below, and the full list consid-
 709 ered is described in detail in the associated paper [8]. These uncertainties cover

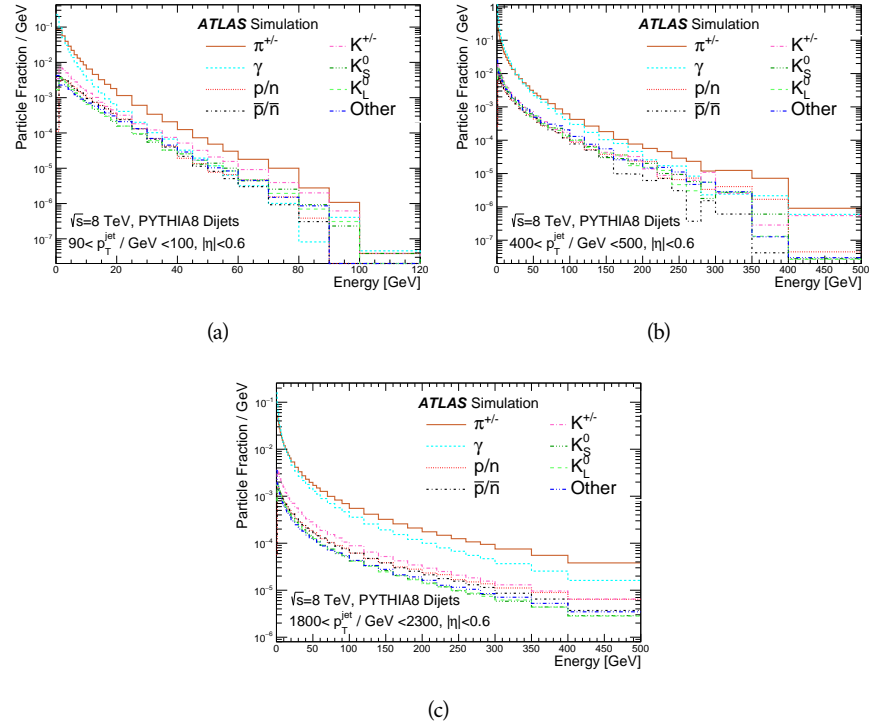


Figure 19: The spectra of true particles inside anti- k_t , $R = 0.4$ jets with (a) $90 < p_T/\text{GeV} < 100$, (b) $400 < p_T/\text{GeV} < 500$, and (c) $1800 < p_T/\text{GeV} < 2300$.

710 differences between the data and simulation in the modeling of calorimeter re-
 711 sponse to a given particle. No uncertainties are added for the difference between
 712 particle composition of jets in data and simulation.

- 713 • The comparison of $\langle E/p \rangle_{\text{COR}}$ as described in Chapter 8 with statistical
 714 uncertainties from 500 MeV to 20 GeV (“In situ E/p ”).
- 715 • The main $\langle E/p \rangle$ comparison uncertainties, binned in p and $|\eta|$, as derived
 716 from the combined test beam results, from 20 to 350 GeV (“CTB” from
 717 Ref. [10]).
- 718 • The difference in the zero-fraction between data and MC simulation from
 719 500 MeV to 20 GeV (“ E/p Zero Fraction”).
- 720 • The uncertainty in the EM calorimeter response from the potential mis-
 721 modelling of threshold effects in topological clustering (“ E/p Threshold”).
- 722 • The uncertainty in the calorimeter response to neutral hadrons based on
 723 studies of physics model variations (“Neutral”).
- 724 • An additional uncertainty in the response to neutral K_L in the calorimeter
 725 based on studies of physics model variations (“ K_L ”).
- 726 • The uncertainty in the p measurement from misalignment of the ID (“ E/p
 727 Misalignment”).

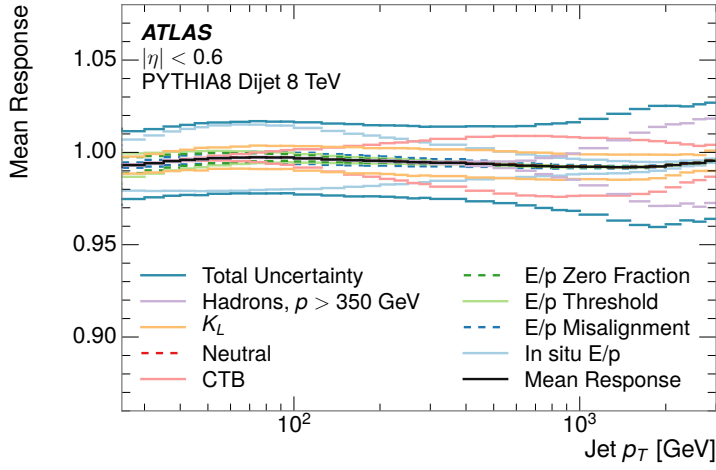
- 728 • A flat uncertainty for all particles above the energy range or outside the
 729 longitudinal range probed with the combined test beam (“Hadrons, $p >$
 730 350 GeV”).

731 From these terms, the jet energy scale and uncertainty is built up from individual
 732 energy deposits in simulation. Each uncertainty term is treated independently,
 733 and are taken to be gaussian distributed. The resulting scale and uncertainty
 734 is shown in Figure 20, where the mean response is measured relative to the
 735 calibrated energy reported by simulation. The dominant uncertainties come
 736 from the statistical uncertainties on the E/p measurements at lower energies and
 737 the additional uncertainty for out of range measurements at higher energies. The
 738 total uncertainty from this method at intermediate jet energies is comparable to
 739 other simulation-based methods [4] and is about twice as large as in-situ meth-
 740 ods using data [7]. This method is the only one which provides an estimation
 741 above 1.8 TeV, however, and so is still a crucial technique in analyses that search
 742 for very energetic jets.

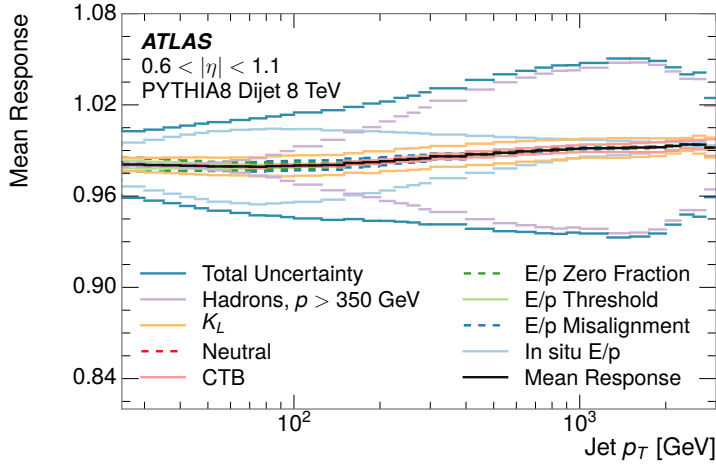
743 These techniques can also be used to measure the correlation between the
 744 average reconstructed jet momentum in a given bin of p_T and $|\eta|$, where cor-
 745 relations are expected because of a similarity in particle composition at similar
 746 energies. Figure 21 shows these correlations, where the uncertainties on jets in
 747 neighboring bins are typically between 30% and 60% correlated. The uncertainty
 748 on all jets becomes significantly correlated at high energies and larger pseudora-
 749 pidities, when the uncertainty becomes dominated by the single term reflecting
 750 out of range particles.

751 9.3 SUMMARY

752 The technique described above provides a jet energy scale and uncertainty by
 753 building up jet corrections from the energy deposits of constituent particles. The
 754 E/p measurements are crucial in providing corrections for the majority of parti-
 755 cles in the jets. The uncertainty derived this way is between 2 and 5% and is about
 756 twice as large at corresponding momentum than jet balance methods. However
 757 this is the only uncertainty available for very energetic jets using 2012 data and
 758 simulation, and repeating this method with Run 2 data and simulation will be
 759 important in providing an uncertainty for the most energetic jets in 13 TeV col-
 760 lisions.



(a)



(b)

Figure 20: The jet energy scale uncertainty contributions, as well as the total jet energy scale uncertainty, as a function of jet p_T for (a) $|\eta| < 0.6$ and (b) $0.6 < |\eta| < 1.1$.

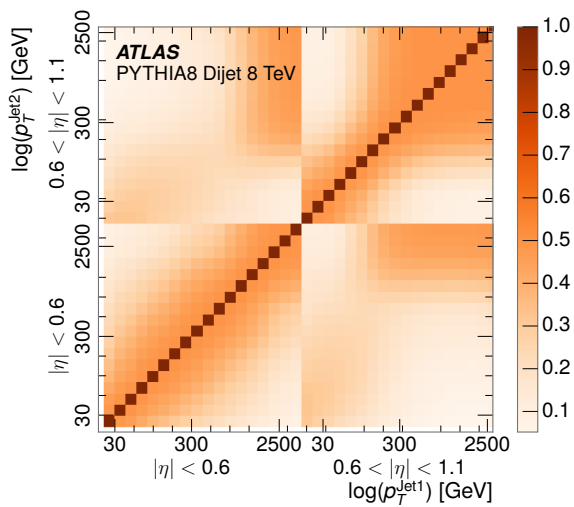


Figure 21: The jet energy scale correlations as a function of jet p_T and $|\eta|$ for jets in the central region of the detector.

761

PART V

762

SEARCH FOR LONG-LIVED PARTICLES

763

You can put some informational part preamble text here.

10

764

765 LONG-LIVED PARTICLES IN ATLAS

766 10.1 OVERVIEW AND CHARACTERISTICS

767 10.2 SIMULATION

768

769 EVENT SELECTION

770 11.1 TRIGGER

771 11.2 KINEMATICS AND ISOLATION

772 11.3 STANDARD MODEL REJECTION

773 11.4 IONIZATION

774 11.4.1 DE/DX CALIBRATION

775 11.4.2 MASS ESTIMATION

12

776

777 BACKGROUND ESTIMATION

778 12.1 BACKGROUND SOURCES

779 12.2 PREDICTION METHOD

780 12.3 VALIDATION AND UNCERTAINTY

13

781

782 SYSTEMATIC UNCERTAINTIES AND RESULTS

783 13.1 SYSTEMATIC UNCERTAINTIES

784 13.2 FINAL YIELDS

14

785

786 INTERPRETATION

787 14.1 CROSS SECTIONAL LIMITS

788 14.2 MASS LIMITS

789 14.3 CONTEXT FOR LONG-LIVED SEARCHES

790

PART VI

791

CONCLUSIONS

792

You can put some informational part preamble text here.

15

793

794 SUMMARY AND OUTLOOK

795 15.1 SUMMARY

796 15.2 OUTLOOK

797

PART VII

798

APPENDIX

799

800

801 INELASTIC CROSS SECTION

A

B

802

803 APPENDIX TEST

804 Examples: *Italics*, SMALL CAPS, ALL CAPS ¹. Acronym testing: **UML!** (**UML!**) –
805 **UML! – UML! (UML!) – UML!s**

This appendix is temporary and is here to be used to check the style of the document.

806 B.1 APPENDIX SECTION TEST

807 Random text that should take up a few lines. The purpose is to see how sections
808 and subsections flow with some actual context. Without some body copy be-
809 tween each heading it can be difficult to tell if the weight of the fonts, styles,
810 and sizes use work well together.

811 B.1.1 APPENDIX SUBECTION TEST

812 Random text that should take up a few lines. The purpose is to see how sections
813 and subsections flow with some actual context. Without some body copy be-
814 tween each heading it can be difficult to tell if the weight of the fonts, styles,
815 and sizes use work well together.

816 B.2 A TABLE AND LISTING

817 Curabitur tellus magna, porttitor a, commodo a, commodo in, tortor. Donec in-
818 terdum. Praesent scelerisque. Maecenas posuere sodales odio. Vivamus metus la-
819 cus, varius quis, imperdiet quis, rhoncus a, turpis. Etiam ligula arcu, elementum a,
820 venenatis quis, sollicitudin sed, metus. Donec nunc pede, tincidunt in, venenatis
821 vitae, faucibus vel, nibh. Pellentesque wisi. Nullam malesuada. Morbi ut tellus ut
822 pede tincidunt porta. Lorem ipsum dolor sit amet, consectetur adipiscing elit.
823 Etiam congue neque id dolor.

824 There is also a Python listing below Listing 1.

1 Footnote example.

LABITUR BONORUM PRI NO	QUE VISTA	HUMAN
fastidii ea ius	germano	demonstratea
suscipit instructior	titulo	personas
quaestio philosophia	facto	demonstrated

Table 1: Autem usu id.

825 B.3 SOME FORMULAS

Due to the statistical nature of ionisation energy loss, large fluctuations can occur in the amount of energy deposited by a particle traversing an absorber element². Continuous processes such as multiple scattering and energy loss play a relevant role in the longitudinal and lateral development of electromagnetic and hadronic showers, and in the case of sampling calorimeters the measured resolution can be significantly affected by such fluctuations in their active layers. The description of ionisation fluctuations is characterised by the significance parameter κ , which is proportional to the ratio of mean energy loss to the maximum allowed energy transfer in a single collision with an atomic electron:

You might get unexpected results using math in chapter or section heads. Consider the pdfspacing option.

$$\kappa = \frac{\xi}{E_{\max}} \quad (1)$$

E_{\max} is the maximum transferable energy in a single collision with an atomic electron.

$$E_{\max} = \frac{2m_e\beta^2\gamma^2}{1 + 2\gamma m_e/m_x + (m_e/m_x)^2},$$

826 where $\gamma = E/m_x$, E is energy and m_x the mass of the incident particle, $\beta^2 =$
 827 $1 - 1/\gamma^2$ and m_e is the electron mass. ξ comes from the Rutherford scattering
 828 cross section and is defined as:

$$\xi = \frac{2\pi z^2 e^4 N_{Av} Z \rho \delta x}{m_e \beta^2 c^2 A} = 153.4 \frac{z^2}{\beta^2} \frac{Z}{A} \rho \delta x \text{ keV},$$

829 where

830 z charge of the incident particle
 830 N_{Av} Avogadro's number
 830 Z atomic number of the material
 830 A atomic weight of the material
 830 ρ density
 830 δx thickness of the material
 831 κ measures the contribution of the collisions with energy transfer close to
 832 E_{\max} . For a given absorber, κ tends towards large values if δx is large and/or if
 833 β is small. Likewise, κ tends towards zero if δx is small and/or if β approaches
 834 1.

2 Examples taken from Walter Schmidt's great gallery:
<http://home.vrweb.de/~was/mathfonts.html>

Listing 1: A floating example (listings manual)

```
1 for i in xrange(10):
    print i, i*i, i*i*i
print "done"
```

835 The value of κ distinguishes two regimes which occur in the description of
836 ionisation fluctuations:

- 837 1. A large number of collisions involving the loss of all or most of the incident
838 particle energy during the traversal of an absorber.

839 As the total energy transfer is composed of a multitude of small energy
840 losses, we can apply the central limit theorem and describe the fluctua-
841 tions by a Gaussian distribution. This case is applicable to non-relativistic
842 particles and is described by the inequality $\kappa > 10$ (i. e., when the mean
843 energy loss in the absorber is greater than the maximum energy transfer
844 in a single collision).

- 845 2. Particles traversing thin counters and incident electrons under any condi-
846 tions.

847 The relevant inequalities and distributions are $0.01 < \kappa < 10$, Vavilov
848 distribution, and $\kappa < 0.01$, Landau distribution.

- 850 [1] ATLAS Collaboration. “The ATLAS Simulation Infrastructure”. In: *Eur.*
851 *Phys. J. C* 70 (2010), p. 823. doi: [10.1140/epjc/s10052-010-1429-9](https://doi.org/10.1140/epjc/s10052-010-1429-9).
852 arXiv: [1005.4568 \[hep-ex\]](https://arxiv.org/abs/1005.4568). SOFT-2010-01.
- 853 [2] ATLAS Collaboration. “A study of the material in the ATLAS inner de-
854 tector using secondary hadronic interactions”. In: *JINST* 7 (2012), P01013.
855 doi: [10.1088/1748-0221/7/01/P01013](https://doi.org/10.1088/1748-0221/7/01/P01013). arXiv: [1110.6191 \[hep-ex\]](https://arxiv.org/abs/1110.6191).
856 PERF-2011-08.
- 857 [3] ATLAS Collaboration. *Summary of ATLAS Pythia 8 tunes*. ATL-PHYS-PUB-
858 2012-003. 2012. url: <http://cds.cern.ch/record/1474107>.
- 859 [4] ATLAS Collaboration. “Jet energy measurement with the ATLAS detector
860 in proton–proton collisions at $\sqrt{s} = 7$ TeV”. In: *Eur. Phys. J. C* 73 (2013),
861 p. 2304. doi: [10.1140/epjc/s10052-013-2304-2](https://doi.org/10.1140/epjc/s10052-013-2304-2). arXiv: [1112.6426 \[hep-ex\]](https://arxiv.org/abs/1112.6426). PERF-2011-03.
- 863 [5] ATLAS Collaboration. “Single hadron response measurement and calorime-
864 ter jet energy scale uncertainty with the ATLAS detector at the LHC”. In:
865 *Eur. Phys. J. C* 73 (2013), p. 2305. doi: [10.1140/epjc/s10052-013-2305-1](https://doi.org/10.1140/epjc/s10052-013-2305-1). arXiv: [1203.1302 \[hep-ex\]](https://arxiv.org/abs/1203.1302). PERF-2011-05.
- 867 [6] ATLAS Collaboration. “Electron and photon energy calibration with the
868 ATLAS detector using LHC Run 1 data”. In: *Eur. Phys. J. C* 74 (2014), p. 3071.
869 doi: [10.1140/epjc/s10052-014-3071-4](https://doi.org/10.1140/epjc/s10052-014-3071-4). arXiv: [1407.5063 \[hep-ex\]](https://arxiv.org/abs/1407.5063). PERF-2013-05.
- 871 [7] ATLAS Collaboration. “Jet energy measurement and its systematic uncer-
872 tainty in proton–proton collisions at $\sqrt{s} = 7$ TeV with the ATLAS detec-
873 tor”. In: *Eur. Phys. J. C* 75 (2015), p. 17. doi: [10.1140/epjc/s10052-014-3190-y](https://doi.org/10.1140/epjc/s10052-014-3190-y). arXiv: [1406.0076 \[hep-ex\]](https://arxiv.org/abs/1406.0076). PERF-2012-01.
- 875 [8] ATLAS Collaboration. “A measurement of the calorimeter response to sin-
876 ggle hadrons and determination of the jet energy scale uncertainty using
877 LHC Run-1 pp -collision data with the ATLAS detector”. In: (2016). arXiv:
878 [1607.08842 \[hep-ex\]](https://arxiv.org/abs/1607.08842). PERF-2015-05.
- 879 [9] ATLAS Collaboration. “Topological cell clustering in the ATLAS calorime-
880 ters and its performance in LHC Run 1”. In: (2016). arXiv: [1603.02934](https://arxiv.org/abs/1603.02934)
881 [hep-ex].
- 882 [10] E. Abat et al. “Study of energy response and resolution of the ATLAS barrel
883 calorimeter to hadrons of energies from 20 to 350 GeV”. In: *Nucl. Instrum.*
884 *Meth. A* 621.1-3 (2010), pp. 134 – 150. doi: <http://dx.doi.org/10.1016/j.nima.2010.04.054>.

- 886 [11] P. Adragna et al. "Measurement of Pion and Proton Response and Lon-
 887 gitudinal Shower Profiles up to 20 Nuclear Interaction Lengths with the
 888 ATLAS Tile Calorimeter". In: *Nucl. Instrum. Meth. A* 615 (2010), pp. 158–
 889 181. doi: [10.1016/j.nima.2010.01.037](https://doi.org/10.1016/j.nima.2010.01.037).
- 890 [12] S. Agostinelli et al. "GEANT4: A simulation toolkit". In: *Nucl. Instrum. Meth.*
 891 A 506 (2003), pp. 250–303. doi: [10.1016/S0168-9002\(03\)01368-8](https://doi.org/10.1016/S0168-9002(03)01368-8).
- 892 [13] N. S. Amelin et al. "Transverse flow and collectivity in ultrarelativistic
 893 heavy-ion collisions". In: *Phys. Rev. Lett.* 67 (1991), p. 1523. doi: [10.1103/PhysRevLett.67.1523](https://doi.org/10.1103/PhysRevLett.67.1523).
- 895 [14] N. S. Amelin et al. "Collectivity in ultrarelativistic heavy ion collisions". In:
 896 *Nucl. Phys. A* 544 (1992), p. 463. doi: [10.1016/0375-9474\(92\)90598-E](https://doi.org/10.1016/0375-9474(92)90598-E).
- 898 [15] B. Andersson, A. Tai, and B.-H. Sa. "Final state interactions in the (nuclear)
 899 FRITIOF string interaction scenario". In: *Z. Phys. C* 70 (1996), pp. 499–
 900 506. doi: [10.1007/s002880050127](https://doi.org/10.1007/s002880050127).
- 901 [16] B. Andersson et al. "A model for low-pT hadronic reactions with general-
 902 izations to hadron-nucleus and nucleus-nucleus collisions". In: *Nucl. Phys.*
 903 B 281 (1987), p. 289. doi: [10.1016/0550-3213\(87\)90257-4](https://doi.org/10.1016/0550-3213(87)90257-4).
- 904 [17] H. W. Bertini and P. Guthrie. "News item results from medium-energy
 905 intranuclear-cascade calculation". In: *Nucl. Instr. and Meth. A* 169 (1971),
 906 p. 670. doi: [10.1016/0375-9474\(71\)90710-X](https://doi.org/10.1016/0375-9474(71)90710-X).
- 907 [18] L. V. Bravin et al. "Scaling violation of transverse flow in heavy ion col-
 908 lisions at AGS energies". In: *Phys. Lett. B* 344 (1995), p. 49. doi: [10.1016/0370-2693\(94\)01560-Y](https://doi.org/10.1016/0370-2693(94)01560-Y).
- 910 [19] L. V. Bravina et al. "Fluid dynamics and Quark Gluon string model - What
 911 we can expect for Au+Au collisions at 11.6 AGeV/c". In: *Nucl. Phys. A* 566
 912 (1994), p. 461. doi: [10.1016/0375-9474\(94\)90669-6](https://doi.org/10.1016/0375-9474(94)90669-6).
- 913 [20] CMS Collaboration. "The CMS barrel calorimeter response to particle
 914 beams from 2 to 350 GeV/c". In: *Eur. Phys. J. C* 60.3 (2009). doi: [10.1140/epjc/s10052-009-0959-5](https://doi.org/10.1140/epjc/s10052-009-0959-5).
- 916 [21] H. S. Fesefeldt. *GHEISHA program*. Pitha-85-02, Aachen. 1985.
- 917 [22] G. Folger and J.P. Wellisch. "String parton models in Geant4". In: (2003).
 918 arXiv: [nucl-th/0306007](https://arxiv.org/abs/nucl-th/0306007).
- 919 [23] B. Ganhuyag and V. Uzhinsky. "Modified FRITIOF code: Negative charged
 920 particle production in high energy nucleus nucleus interactions". In: *Czech.
 921 J. Phys.* 47 (1997), pp. 913–918. doi: [10.1023/A:1021296114786](https://doi.org/10.1023/A:1021296114786).
- 922 [24] M. P. Guthrie, R. G. Alsmiller, and H. W. Bertini. "Calculation of the cap-
 923 ture of negative pions in light elements and comparison with experiments
 924 pertaining to cancer radiotherapy". In: *Nucl. Instrum. Meth.* 66 (1968), pp. 29–
 925 36. doi: [10.1016/0029-554X\(68\)90054-2](https://doi.org/10.1016/0029-554X(68)90054-2).
- 926 [25] J. Beringer et al. (Particle Data Group). "Review of Particle Physics". In:
 927 *Chin. Phys. C* 38 (2014), p. 090001. URL: <http://pdg.lbl.gov>.

- 928 [26] V.A. Karmanov. "Light Front Wave Function of Relativistic Composite
929 System in Explicitly Solvable Model". In: *Nucl. Phys. B* 166 (1980), p. 378.
930 doi: [10.1016/0550-3213\(80\)90204-7](https://doi.org/10.1016/0550-3213(80)90204-7).
- 931 [27] Hung-Liang Lai, Marco Guzzi, Joey Huston, Zhao Li, Pavel M. Nadolsky,
932 et al. "New parton distributions for collider physics". In: *Phys. Rev. D* 82
933 (2010), p. 074024. doi: [10.1103/PhysRevD.82.074024](https://doi.org/10.1103/PhysRevD.82.074024). arXiv: [1007.2241 \[hep-ph\]](https://arxiv.org/abs/1007.2241).
- 935 [28] A.D. Martin, W.J. Stirling, R.S. Thorne, and G. Watt. "Parton distributions
936 for the LHC". In: *Eur. Phys. J. C* 63 (2009). Figures from the [MSTW Website](#),
937 pp. 189–285. doi: [10.1140/epjc/s10052-009-1072-5](https://doi.org/10.1140/epjc/s10052-009-1072-5). arXiv: [0901.0002](https://arxiv.org/abs/0901.0002).
- 939 [29] B. Nilsson-Almqvist and E. Stenlund. "Interactions Between Hadrons and
940 Nuclei: The Lund Monte Carlo, Fritiof Version 1.6". In: *Comput. Phys. Com-*
941 *mun.* 43 (1987), p. 387. doi: [10.1016/0010-4655\(87\)90056-7](https://doi.org/10.1016/0010-4655(87)90056-7).
- 942 [30] A. Ribon et al. *Status of Geant4 hadronic physics for the simulation of LHC*
943 *experiments at the start of LHC physics program*. CERN-LCGAPP-2010-02.
944 2010. URL: <http://lcgapp.cern.ch/project/docs/noteStatusHadronic2010.pdf>.
- 946 [31] A. Sherstnev and R.S. Thorne. "Parton Distributions for LO Generators".
947 In: *Eur. Phys. J. C* 55 (2008), pp. 553–575. doi: [10.1140/epjc/s10052-008-0610-x](https://doi.org/10.1140/epjc/s10052-008-0610-x). arXiv: [0711.2473](https://arxiv.org/abs/0711.2473).
- 949 [32] T. Sjöstrand, S. Mrenna, and P. Skands. "A Brief Introduction to PYTHIA
950 8.1". In: *Comput. Phys. Commun.* 178 (2008), pp. 852–867. doi: [10.1016/j.cpc.2008.01.036](https://doi.org/10.1016/j.cpc.2008.01.036). arXiv: [0710.3820](https://arxiv.org/abs/0710.3820).
- 952 [33] Peter Speckmayer. "Energy Measurement of Hadrons with the CERN AT-
953 LAS Calorimeter". Presented on 18 Jun 2008. PhD thesis. Vienna: Vienna,
954 Tech. U., 2008. URL: <http://cds.cern.ch/record/1112036>.

955 DECLARATION

956 Put your declaration here.

957 *Berkeley, CA, September 2016*

958

Bradley Axen

959

960 COLOPHON

961

Not sure that this is necessary.